Nanoscale

Flexible All-Solid-State Supercapacitor Based on Carbon-Supported Ni-Embedded Boron Nitride

Journal:	*Nanoscale*
Manuscript ID	NR-ART-05-2025-001926.R1
Article Type:	Paper
Date Submitted by the Author:	29-May-2025

Complete List of Authors:	De, Shrabani; North Carolina A&T State University, Department of Chemistry Raj, Binod; North Carolina Agricultural and Technical State University Pathiraja, Gayani; The University of North Carolina at Greensboro, Nanoscience; The University of North Carolina at Greensboro, Bastakoti, Bishnu; North Carolina A&T State University, Department of Chemistry

SCHOLARONE™
Manuscripts

Flexible All-Solid-State Supercapacitor Based on Carbon-Supported Ni-Embedded Boron Nitride

Shrabani De[a], Binod Raj KC[a], Gayani Pathiraja[b], Bishnu Prasad Bastakoti[a*]

[a]Department of Chemistry, North Carolina A&T State University, 1601 E. Market St. Greensboro, NC 27411 (USA)

[b]Department of Nanoscience, Joint School of Nanoscience and Nanoengineering, University of North Carolina at Greensboro, 2907 East Gate City Blvd, Greensboro, NC 27401 (USA)

*Email: bpbastakoti@ncat.edu

Abstract

It is challenging to identify alternative uses for hazardous pollutant materials that can benefit the environment. Non-biodegradable, toxic waste cigarette filters can be used as a good source of low-cost carbon for electrode materials. A new combination of Ni-embedded boron nitride (BN) with carbon derived from cigarette filters is reported as an efficient electrode for a flexible all-solid-state asymmetric supercapacitor. The incorporation of nickel nanoparticles inside BN nanosheets helps to restrict their layer stacking tendency and induce redox-active centres in 2D layers which tune their electrochemical properties. The incorporation of a conducting carbon backbone into the Ni-embedded boron nitride facilitates electron transfer pathways, thereby enhancing its electrochemical performance. The fabricated all-solid-state asymmetric supercapacitor exhibited excellent flexibility and durability up to 250 bending cycles. The device exhibited high specific capacitance, power density, and energy density of 47 F g^{-1}, 4395.7 W kg^{-1}, and 7.9 Wh kg^{-1}, respectively, with a volumetric energy density of 0.25 mWh cm^{-3} at 2 A g^{-1}. The device exhibited excellent cyclic stability, with 86% specific capacitance retention after 10,000 charging-discharging cycles. The real-time application of the flexible device was also tested by glowing up a red LED. The described method will pave the way for waste management to become a flexible energy storage material. This study reports such a unique combination of waste cigarette filter-derived carbon-supported Ni-embedded BN for flexible supercapacitors.

Keywords: Boron nitride, nickel nanoparticles, waste cigarette filter-derived carbon, all-solid-state flexible asymmetric supercapacitor, waste-to-energy

1. Introduction

The increasing demand for energy and the urgent need to reduce air pollution caused by reliability on fossil fuels have prompted increased efforts to capture and store renewable energy. In place of fossil fuels, renewable energy sources such as solar, wind, and hydroelectric power provide sustainable, clean, and environmentally friendly alternatives. However, due to their sporadic nature, efficient energy storage systems are necessary to ensure grid stability and a consistent supply. Supercapacitors have shown promise as potential solutions to these problems. Supercapacitors offer unique benefits and can be broadly divided into two types: electrical double-layer capacitors (EDLCs) and pseudocapacitors. High power density and cyclic stability are characteristics of EDLCs, which are usually made of carbonaceous materials[1]. On the other hand, pseudocapacitors, which comprise reversible redox centres, have comparatively higher energy densities and high capacitance[2-5]. The goal of recent research has been to merge these two different material types into a single device to maximize their combined benefits and open the door for broad use in a range of energy storage applications[6-10]. The energy storage research community actively seeks new materials systems that can endure extreme conditions, such as high mass loading, high charge-discharge cycling rates and stability, severe electrolytic environments, and elevated heat conditions. Carbon, two-dimensional (2D) materials, and their related nanohybrids are widely acknowledged as supercapacitor electrodes for their unique properties and structural stability, which make them promising candidates for next-generation energy storage systems[11-17].

One of the 2D materials, hexagonal boron nitride (BN), has a layered sp^2-hybridized structure with considerable structural stability even at high temperatures (having a melting point of >2900 °C), lightweight nature (with density of ~2.1 g cm^{-3}), high thermal conductivity of > 250 W mK^{-1}, and remarkable flexibility (having a Young's modulus >0.85 TPa and a fracture strength of >70 GPa)[18]. Also, BN exhibited excellent stability under various electrolytic conditions. Despite these advantageous characteristics, BN is not suitable for use as an electrode material in its pristine form because of its wide electronic band gap of ~4–6 eV, and poor electrical conductivity[19]. However, doping, functionalization, and interface engineering can remarkably tune their electronic band gap and increase their conductivity, widening their potential applications in electrochemical energy storage devices[19-23].

Doping BN with transition metals offers a promising approach to enhance its electrical conductivity and reduce its band gap, thereby increasing its electrochemical activity. Numerous

theoretical studies have demonstrated that transition metal doping can successfully modify the physical, electrical, and magnetic characteristics of BN[24-26]. Recently, very few experimental studies have been reported on transition metal-infused BN. For example, Fe-doped BN was reported by Joy et al. via a microwave-assisted pathway and this Fe-doped BN modified with conducting polymer delivered efficient supercapacitor performance with 15.25 Wh kg^{-1} energy density at 2 A g^{-1}[19]. In another study, Ikram et al. prepared Ni-doped BN via hydrothermal method by mixing BN with $NiCl_2$ and exhibited that doping enhanced its catalytic activity towards dye degradation[27]. However, there are no reports of metal nanoparticle-embedded boron nitride synthesized via the solid-state method.

The incorporation of conducting fillers also helps to overcome their electrochemical limitations by forming an intimate and synergistic heterojunction, which facilitates easy electron transfer, leading to enhanced current response and overall electrochemical efficiency of BN-based materials. In this context, reduced graphene oxide and carbonaceous materials have been widely explored as filler materials due to their high electrical conductivity. Saha et al. introduced reduced graphene oxide within hexagonal-BN to increase its electrical conductivity, leading to the enhancement in electrochemical performance with high specific capacitance of 145.7 F g^{-1} and large energy density of 39.6 Wh kg^{-1}[28]. In another study, Li et al. reported a carbon-modified BN nanosheet (h-BN/C) with enhanced electrical conductivity and high surface area. The h-BN/C nanocomposite was used as a positive electrode for the asymmetric supercapacitor, which displayed a wide voltage window of 1.45 V with high energy density and power density of 17 Wh kg^{-1} and 245 W kg^{-1}, respectively, with high stability up to 1000 cycles[29].

Particularly, the consumption of waste material-derived carbon as an electrode for energy storage devices has garnered considerable attention due to its multifaceted benefits, ranging from waste management to combating the energy crisis. Used cigarette filters are regarded as a serious pollutant, as they are non-biodegradable and toxic to freshwater and soil. Globally, the annual cigarette consumption statistics are around 5.8 trillion. The conversion of chemicals present in cigarette filters, including cellulose acetate, paper, rayon, and other additives, into carbon not only reduces pollution but also produces low-cost electroactive material for supercapacitors. Wu et al. reported activated carbon derived from waste cigarette filters as an efficient electrode for flexible capacitive supercapacitor with high specific capacitance (106.5 F g^{-1}) and energy density (5.15 Wh kg^{-1})[31]. In another report, Bi et al. showed cigarette filter-derived porous activated carbon as a sustainable energy source[32]. The

symmetric supercapacitor assembled using porous activated carbon delivered a large specific capacitance (52 F g^{-1}), energy density (7.2 Wh kg^{-1}), power density (127 W kg^{-1}), and excellent cyclic stability with 97.2% retention up to 5000 cycles. However, used cigarette filter-derived carbon has not been studied combined with less conducting BN as an electroactive material for supercapacitor.

Encouraged by the concept of waste-to-energy and the opportunity to convert an insulator material, BN, into an efficient electroactive composite, a solid-state synthesis method is proposed for designing Ni-embedded BN, combined with used cigarette filter-derived carbon, studied as an efficient electrode for a flexible all-solid-state asymmetric supercapacitor. The incorporation of nickel nanoparticles inside BN nanosheets induces redox-active centres (Ni^{2+}/Ni^{3+}) in 2D layers which tune their electrochemical properties. The integration of the conducting carbon matrix to the Ni-embedded boron nitride facilitates the electron transfer pathways and restricts the layer stacking of BN layers which reduces the volume expansion and triggers its electrochemical performance. The heterojunctions generated within Ni, BN nanosheets, and carbon systems facilitate electron transport between the electrode-electrolyte interface. This study reports a unique combination of a used cigarette filter-derived carbon-supported Ni-embedded BN for flexible supercapacitors, paving the way for waste management as an electroactive material.

2. Experimental Section

2.1. Materials

All the chemicals used in the studies were analytical grade and used without any additional processing. Used cigarette (Marlboro, USA) filters have been collected. Boric acid (H_3BO_3) was purchased from Merck, USA, urea ($CO(NH_2)_2$) was acquired from ACROS ORGANICS, USA, and Nickel (II) chloride hexahydrate (98+%) was obtained from thermo scientific, USA. Polyvinyl alcohol (PVA, 98–99%, high molecular weight), ethanol (96%, v/v), and potassium hydroxide (KOH) were obtained from Thermo Fisher Scientific, USA.

2.2. Characterizations

The crystal structure of the prepared samples was analysed via X-ray diffraction (XRD) analysis on a Rigaku MiniFlex 600 with Cu Kα at a wavelength of 1.5406 Å. Morphology and elemental mapping were investigated using field-emission scanning electron microscopy (FESEM) and energy-dispersive X-ray spectroscopy (EDS) mapping, respectively, on a JEOL

JSM-IT800 Schottky instrument. The bulk topography of the sample was studied via high-resolution transmission electron microscopy (HRTEM) on a JEOL 2100PLUS instrument at 200 kV with an EDS facility. Kratos Axis Supra X-ray photoelectron spectroscopy (XPS) was used to characterize the elemental composition and bonding state of the sample. Electrochemical analysis was performed using a BioLogic VSP-50 electrochemical workstation.

2.3. Synthesis

2.3.1. Synthesis of boron nitride (BN): Boron nitride nanosheets were synthesized via solid-state in-situ method. Typically, urea and boric acid were taken in 12:1 weight ratio and dissolved in deionized (DI) water. Then, the solution was kept at 65 °C for recrystallization, and the resulting solid powder was heated at 1000 °C for 5 h under N_2 environment at 5 °C min^{-1} heating rate in a tube furnace. After cooling down to room temperature, the product was washed with water and ethanol by centrifugation to eliminate remaining impurities and dried in a vacuum oven at 60 °C for 12 h.

2.3.2. Synthesis of Ni-doped boron nitride (Ni-BN): For the synthesis of Ni-BN, a similar method was followed with the above-mentioned BN synthesis with the addition of $NiCl_2.6H_2O$ in 1:10 and 1:5 ratio of Ni and BN with the urea and boric acid mixture. The presence of urea helps to reduce Ni^{2+} to Ni^0 at high temperatures. The products were named Ni-BN-1:10 and Ni-BN-1:5, corresponding to the 1:10 and 1:5 ratios of Ni and BN, respectively.

2.3.3. Synthesis of cigarette filter-derived carbon (C): Cigarette filter-derived carbon was synthesized following the standard pyrolysis method. Firstly, the paper wrap was removed from the collected cigarette filters, and they were washed with water and ethanol to remove dust particles. Then, cleaned, dried, and finely chopped cigarette filters were annealed at 800 °C for 3 h under N_2 environment at 5 °C min^{-1} heating rate in a tube furnace.

2.3.4. Synthesis of Ni-BN/C binary composite: To synthesize Ni-BN/C binary composite, Ni-BN-1:10 and washed cigarette filters were dispersed in ethanol and dried to get a homogeneous mixture of Ni-BN-1:10 and cigarette filter. Then, the mixture was annealed at 800 °C for 3 h under N_2 environment at 5 °C min^{-1} heating rate in a tube furnace. The obtained product was named as Ni-BN/C. For comparison, BN was also mixed with cigarette filter and annealed following a similar process, and the product was named BN/C. The schematic representation of the synthesis method of the prepared samples is shown in Fig. 1.

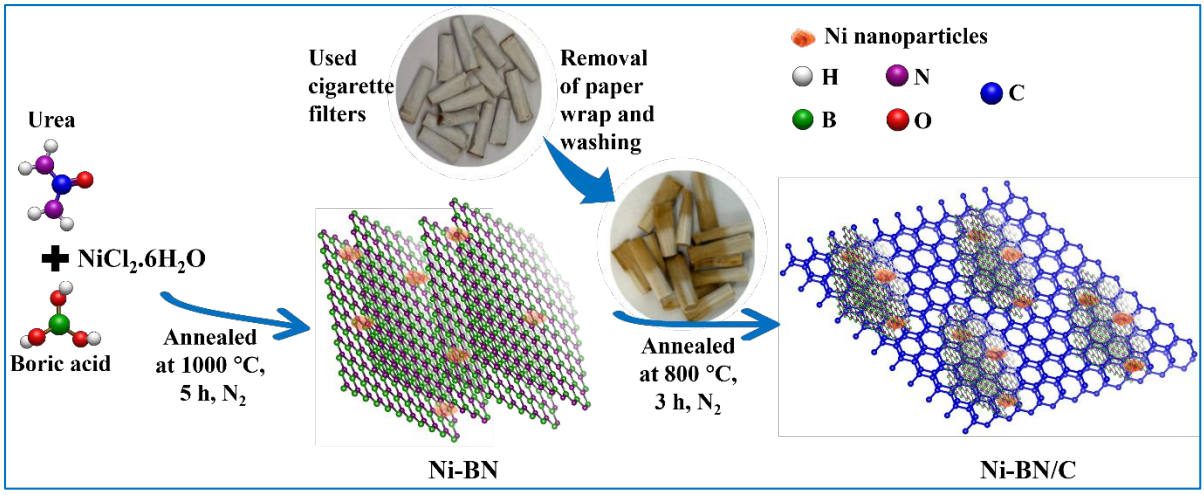

Fig. 1. Schematic illustration of the synthesis of carbon supported Ni-embedded boron nitride.

3. Results and Discussion

3.1. Structural, Compositional, and Morphological Analysis

The structural identification of the synthesized materials with their phase and purity was assessed by powder XRD analysis, as shown in Fig. 2(a). Carbon derived from cigarette filter (C) shows the characteristics of a broad peaks at 2θ = 23°, and 42° corresponding to the (002), and (101) plane of amorphous carbon, respectively[33]. The crystalline peaks at 2θ = 25.3°, and 48° attributed to the quartz particles due to the presence of burned cigarette ash impurities[34]. Boron nitride (BN) nanosheets show characteristic amorphous peaks at 2θ values of 26.27°, and 42.9° corresponding to (002), and (100) planes of BN, respectively[21]. The peak at 26.27° represents the graphite-like structure of BN. The characteristic peaks of BN arise in Ni-BN-1:10 indicating the formation of BN in the presence of nickel. Three extra crystalline peaks at 2θ values of 44.58°, 51.88°, and 76.38° arise in Ni-BN-1:10 attributed to (111), (200), and (222) planes of nickel nanoparticles, respectively due to the fusion of nickel precursor during the BN synthesis[35]. The peak at 26.27° corresponding to (002) plane of BN becomes more intense as FWHM reduces by 2.5° than that of BN because the incorporation of Ni increases the crystallinity of BN. The Ni-BN-1:5 sample exhibits a few additional small peaks, in addition to nickel nanoparticles. The peaks at 2θ = 30.86°, and 55.18° attribute to (002), and (202) planes of Ni_2O_3, respectively, and the peak at 2θ = 49.8° corresponds to (211) plane of NiO[36, 37].

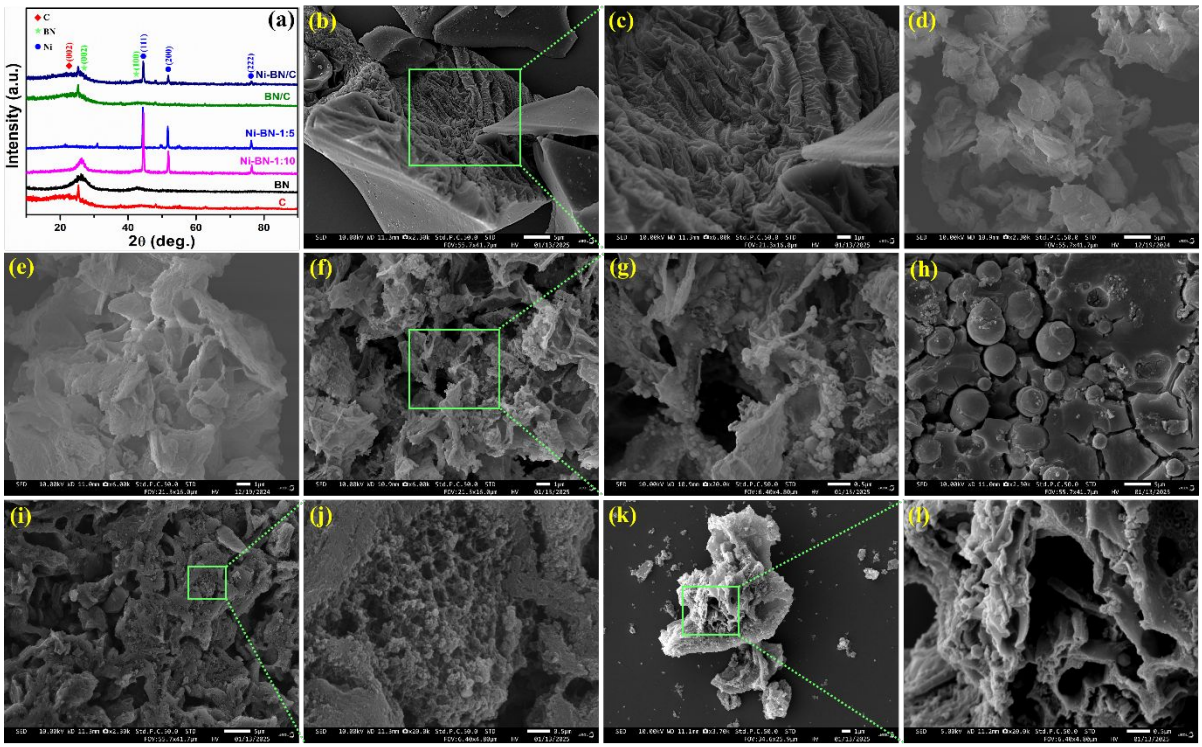

Fig. 2. (a) XRD spectra of C, BN, Ni-BN-1:10, Ni-BN-1:5, BN/C, and Ni-BN/C; FESEM images of (b, c) C, (d, e) BN, (f, g) Ni-BN-1:10, (h) Ni-BN-1:5, (i, j) BN/C, and (k, l) Ni-BN/C.

Also, the characteristic peak of BN is not visible in Ni-BN-1:5 because the formation of BN was abruptly interrupted due to the high concentration of nickel, leading to the formation of boron and nitrogen-doped carbon and nickel nanoparticles along with nickel oxides. Due to the high crystallinity of nickel nanoparticles and nickel oxides, the amorphous carbon peak is not evident in XRD. For BN/C sample the (002) plane of C as well as BN is merged and showed a broad peak at $2\theta = 25.5,^{\circ}$ indicating homogeneous mixing of C and BN during composite formation. Also, the shoulder peak at $2\theta = 43.6^{\circ}$ associated with (100) plane of BN is also observed in BN/C. Additionally, the peaks of quartz impurities coming from burned cigarette ash present in the cigarette filter in BN/C arise at the same 2θ values as C. The Ni-BN/C sample exhibits all the characteristic peaks of C and Ni-BN-1:10, indicating the formation of a binary composite without altering its crystal structure. The distinctive peak for (002) plane of BN becomes a little broader and shifted than the BN/C composite which can be attributed to the presence of Ni particles inside BN sheets, allowing better interaction between BN and C.

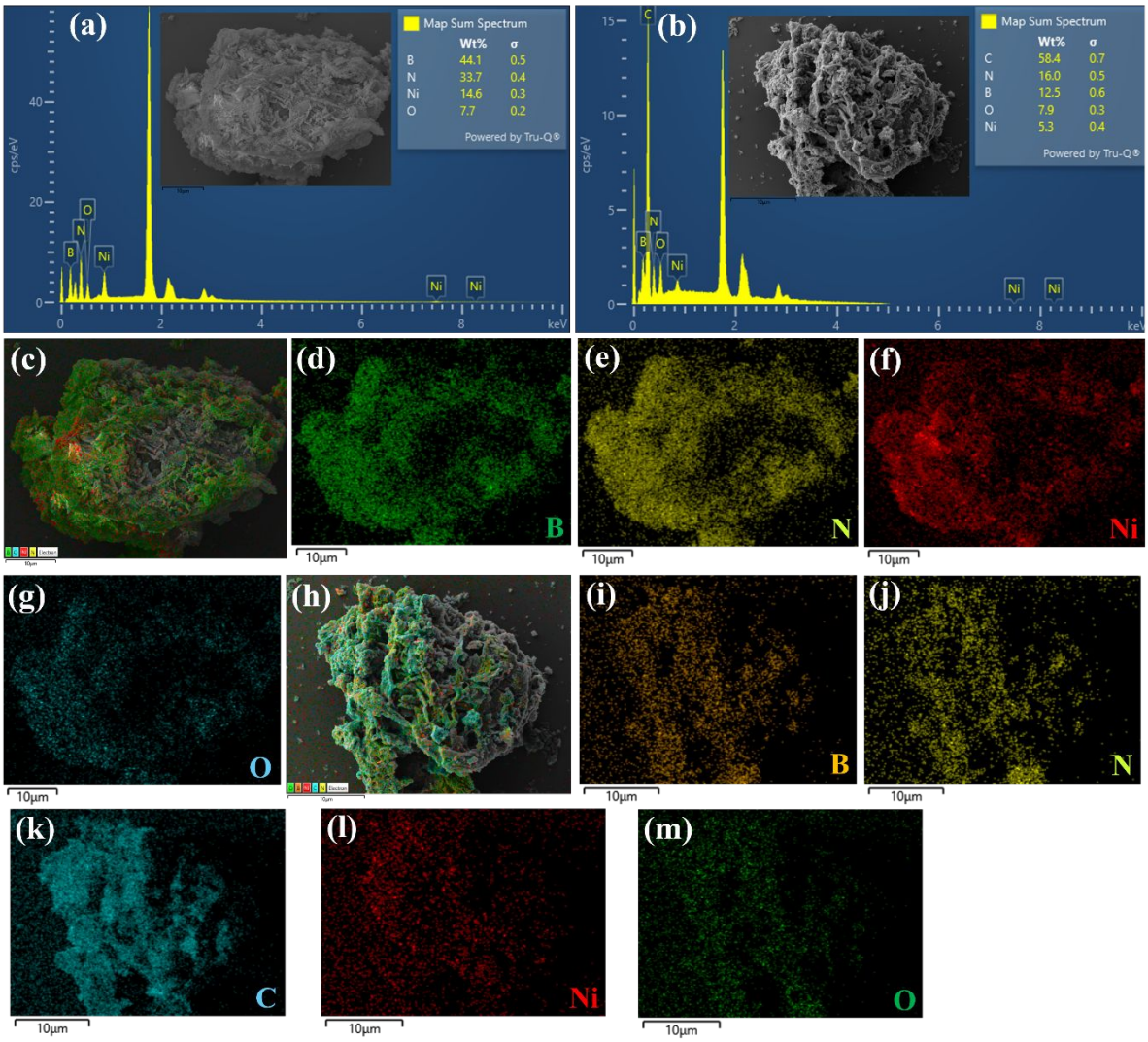

Fig. 3. EDS analysis of (a) Ni-BN-1:10 and (b) Ni-BN/C with percentages of elements present; (c) FESEM overlay map and (d-g) elemental mapping of B, N, Ni, and O of Ni-BN-1:10, respectively; (h) FESEM overlay map and (i-m) elemental mapping of B, N, C, Ni, and O of Ni-BN/C, respectively.

The surface morphology of the synthesized samples was studied via FESEM analysis at different magnifications. The fibrous morphology of the cigarette filter is observed in Fig. S1(a). Fig. 2(b, c) shows the layered sheet-like morphology of cigarette filter-derived C. The delaminated nanosheets of BN are visible from the FESEM image shown in Fig. 2(d, e). The FESEM image of Ni-BN-1:10 is shown in Fig. 2(f, g). It is observed that the Ni nanoparticles infused inside the BN nanosheets indicate homogeneous mixing and growth of Ni nanoparticles inside the BN sheets. The FESEM images of Ni-BN-1:5 shown in Fig. 2(h) and Fig. S1(i) depict that the sheet-like BN morphology is not present, and comparatively big particles of Ni, Ni_2O_3, and NiO are embedded into the B, N-doped carbon structure. This result is also validated and explained by XRD analysis in the above section. Thus, the higher concentration of Ni is

not favourable for BN formation following the same method. The morphology of binary BN/C is shown in Fig. 2(i, j) where a porous morphology resulted from the combination of BN nanosheets and C. Homogeneous mixing of two individual components (BN and C) is assured by no phase separation of individual components and a different type of morphology results after a combination of both components at high temperature. The FESEM images of Ni-BN/C [Fig. 2(k, l)] show porous morphology containing Ni nanoparticle infused BN and C. A uniform combination of Ni-BN-1:10 and C established the good interaction between the components as there is no phase separation of individual components visible.

Further, the EDS analysis [Fig. S1(b)] of cigarette filter reveals the presence of C and O as the primary component. The EDS analysis of BN shows that the weight% of B and N are almost similar, and they are the main component of BN [Fig. S1(c)] nanosheets, while a small amount of C and O is also present in BN as impurities from starting reagents. The elemental mapping of BN [Fig. S1(d-h)] also depicts that BN nanosheets mainly consist of B and N elements, confirming their synthesis. The EDS study of Ni-BN-1:10 [Fig. 3(a)] depicts the presence of Ni in BN and the presence of a small amount of oxygen arises from the starting material impurities of BN. Fig. 3(b) exhibits the EDS analysis of Ni-BN/C showing the presence of C in Ni-BN, indicating the composite formation. The elemental mapping [Fig. 3(c-g)] of Ni-BN-1:10 confirms the infusion of Ni nanoparticles (Ni) in BN nanosheets (B, and N). Fig. 3(h-m) shows the elemental mapping of Ni-BN/C which exhibits uniform mixing of C with Ni-BN-1:10 (Ni, B, and N) assuring a homogeneous composite formation.

The bulk topography of Ni-BN/C was studied using transmission electron microscopy (TEM) analysis as shown in Fig. 4(a, b). It is visible that the Ni particles are embedded inside the BN and C binary sheet-like structure. Most Ni nanoparticles have diameters ranging from 5 to 50 nm. The HRTEM image [Fig. 4(d)] shows the interface between Ni particles and BN/C nanosheets, which is beneficial for facilitating electron transfer and leading to enhanced electrochemical efficiency. The HRTEM fringes arise at two different parts of Fig. 4(d) and are associated with a d-spacing of 0.21 nm [Fig. 4(c)] and 0.34 nm [Fig. 4(e)] attributed to (111) plane of Ni nanoparticles and (002) plane of BN nanosheets, respectively. Further, the selected area electron diffraction (SAED) pattern [Fig. 4(f)] depicts multiple bright spots arranged in ring-like patterns signifying the polycrystalline nature of the sample due to the presence of multiple components. The two prominent rings obtained in the SAED pattern are matched with the corresponding XRD planes which include (111), and (002) planes of Ni nanoparticles. Fig. 4(g-l) exhibits TEM elemental mapping of Ni-BN/C which clearly shows particle-like Ni particles are embedded in BN/C sheets (B, N, C, and O). Also, the

homogeneous distribution of BN and C decorated with Ni signifies good interaction between the individual components and the formation of a homogeneous composite.

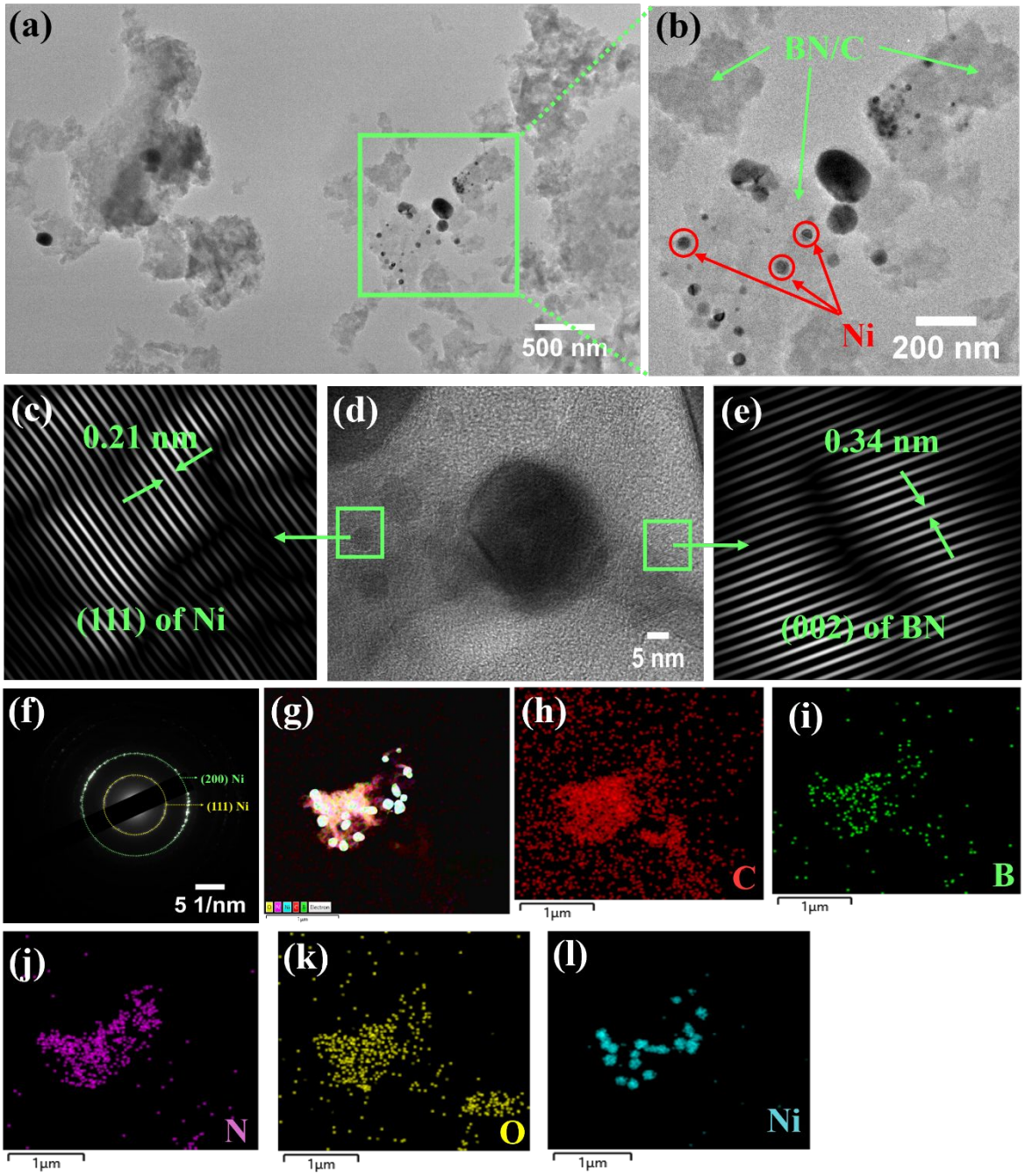

Fig. 4. TEM analysis of Ni-BN/C (a, b) TEM images, (d) HRTEM image, (c) lattice fringes of Ni, (e) lattice fringes of BN, (f) SAED pattern, (g) TEM overlay map, (h-l) elemental mapping of C, B, N, O, and Ni, respectively.

XPS analysis was performed to study chemical states, bonding nature, and surface elemental compositions of Ni-BN/C. A full surface survey scan [Fig. 5 (a)] confirms the presence of C, B, N, O, and Ni in the sample without other impurities. The atomic percentages of each element are listed in Fig. 5(a) inset and the low concentration of Ni supports the fact

that Ni is embedded or infused inside the BN layers which is not fully detected by the surface scan. It is also observed that B and N have the same atomic percentages, indicating the formation of BN. The presence of oxygen comes from the surface oxygen entities and functionalities of BN and C. Fig. 5(b) depicts the deconvoluted XPS spectrum of C 1s consisting of three characteristic peaks at 284.5, 285.8, and 287.4 eV which correspond to C-C, C-O, and C=O bonds, respectively[38]. It signifies that the cigarette filter-derived C contains some oxygen containing surface functionalities. The high-resolution B 1s XPS spectrum [Fig. 5(c)] shows two characteristic peaks at 190.7 and 192.18 eV which attribute to B-N, and B-O, respectively[39]. The B-N bond is slightly shifted towards higher binding energy compared to the pure B-N bond, which generally arises at 190 eV due to the presence of less electronegative Ni compared to B inside BN layers. The B-O bond arises either from starting material (H_3BO_3) impurities or surface oxygen groups. The high-resolution N 1s XPS spectrum [Fig. 5(d)] shows two characteristic peaks at 398.3 and 400 eV which attribute to N-B, and N-H, respectively. The N-H bond arises due to the edge termination which is reflective of reductive ammonia atmosphere[39]. The high-resolution Ni 2p XPS spectrum [Fig. 5(e)] shows Ni^{2+}, and Ni^{3+} states are present with a shake-up satellite. The characteristic peaks at 852.8 and 869.87 eV attribute to $Ni^{2+}{}_{3/2}$ and $Ni^{2+}{}_{1/2}$, respectively, whereas the peaks at 856.17 and 873.8 eV attribute to $Ni^{3+}{}_{3/2}$ and $Ni^{3+}{}_{1/2}$, respectively. The surface nickel hydroxides are the primary source of the Ni^{2+} and Ni^{3+} species on the produced Ni nanoparticles[40]. The high-resolution O 1s XPS spectrum [Fig. 5(f)] shows two characteristic peaks at 532.14 and 533 eV which are attributed to O-B, and O-C bonds, respectively. Therefore, XPS study confirms the presence of Ni^{2+}, and Ni^{3+} states infused in BN which is combined with cigarette filter-derived C.

3.2. Supercapacitor application

The electrochemical performance of the synthesized samples for supercapacitor applications was first optimized via three-electrode analysis in a 1 M KOH electrolyte. The comparison of CV profiles of all the synthesized materials at 50 mV s^{-1} is shown in Fig. 6(a). The CV profiles indicate an electric double layer capacitor (EDLC) type charge storage mechanism for C, BN, BN/C materials due to the absence of any redox peaks. On the other hand, Ni-BN-1:10, Ni-BN-1:5, and Ni-BN/C exhibit deviations from pure EDLC behavior due to the presence of a reversible oxidation-reduction peak. Thus, Ni-BN-1:10, Ni-BN-1:5, and Ni-BN/C samples show both EDLC as well as pseudocapacitance type charge storage mechanisms, where EDLC-like behavior comes from BN layers or porous BN/C, and Ni nanoparticles contribute to the pseudocapacitance. The oxidation peaks of Ni-BN-1:10 and Ni-BN-1:5 arise at around 0.38 V and the reduction peaks arise at around 0.28 V due to the redox couple Ni^{2+}/Ni^{3+}. In KOH

electrolyte, the electrochemical energy storage redox reaction of Ni nanoparticles with surface nickel hydroxides is shown below[40]:

$$Ni(OH)_2 + KOH \leftrightarrow NiOOH + H_2O + e^- + K^+ \quad (1)$$

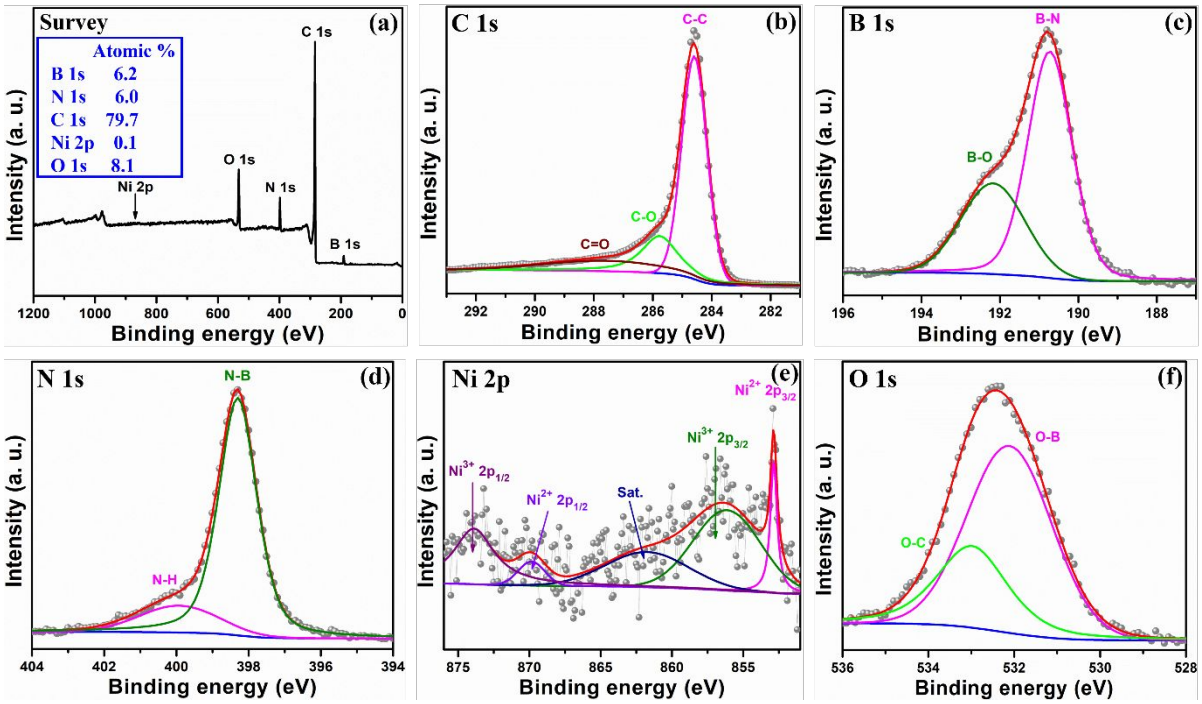

Fig. 5. XPS spectra of Ni-BN/C (a) survey scan, deconvoluted spectra of (b) C 1s, (b) B 1s, (c) N 1s, (d) Ni 2p, and O 1s.

It is interesting to note that the redox peaks of Ni-BN/C composite are slightly shifted towards the right, which can be attributed to the electronic interaction between the components after the incorporation of C within the Ni-BN-1:10. This type of electronic interaction has a significant contribution towards enhancement in electrochemical performance as observed from the CV analysis. Among all the synthesized materials, the highest current response and largest CV area are displayed by Ni-BN/C which can be attributed to the synergistic mixing of C and Ni-BN-1:10, where C provides a conducting backbone to the Ni-embedded BN nanosheets and facilitates the electron transfer between the electrode-electrolyte interface. The comparison of GCD profiles of all the synthesized electrodes at 2.5 A g^{-1} is exhibited in Fig. 6(b). The Ni-BN/C electrode showed the longest discharge time among all the samples which is well in accordance with their CV profiles. The specific capacitance was evaluated from Eq. S1 and Ni-BN/C have the highest specific capacitance of 127.8 F g^{-1} compared to C (2.7 F g^{-1}), BN (4.6 F g^{-1}), Ni-BN-1:5 (9.3 F g^{-1}), Ni-BN-1:10 (13 F g^{-1}), and BN/C (19 F g^{-1}). It is obvious to note that the maximum specific capacitance of Ni-BN/C is associated with the redox contribution of Ni nanoparticles embedded in delaminated BN nanosheets and the conducting C matrix helps to facilitate the electron transfer.

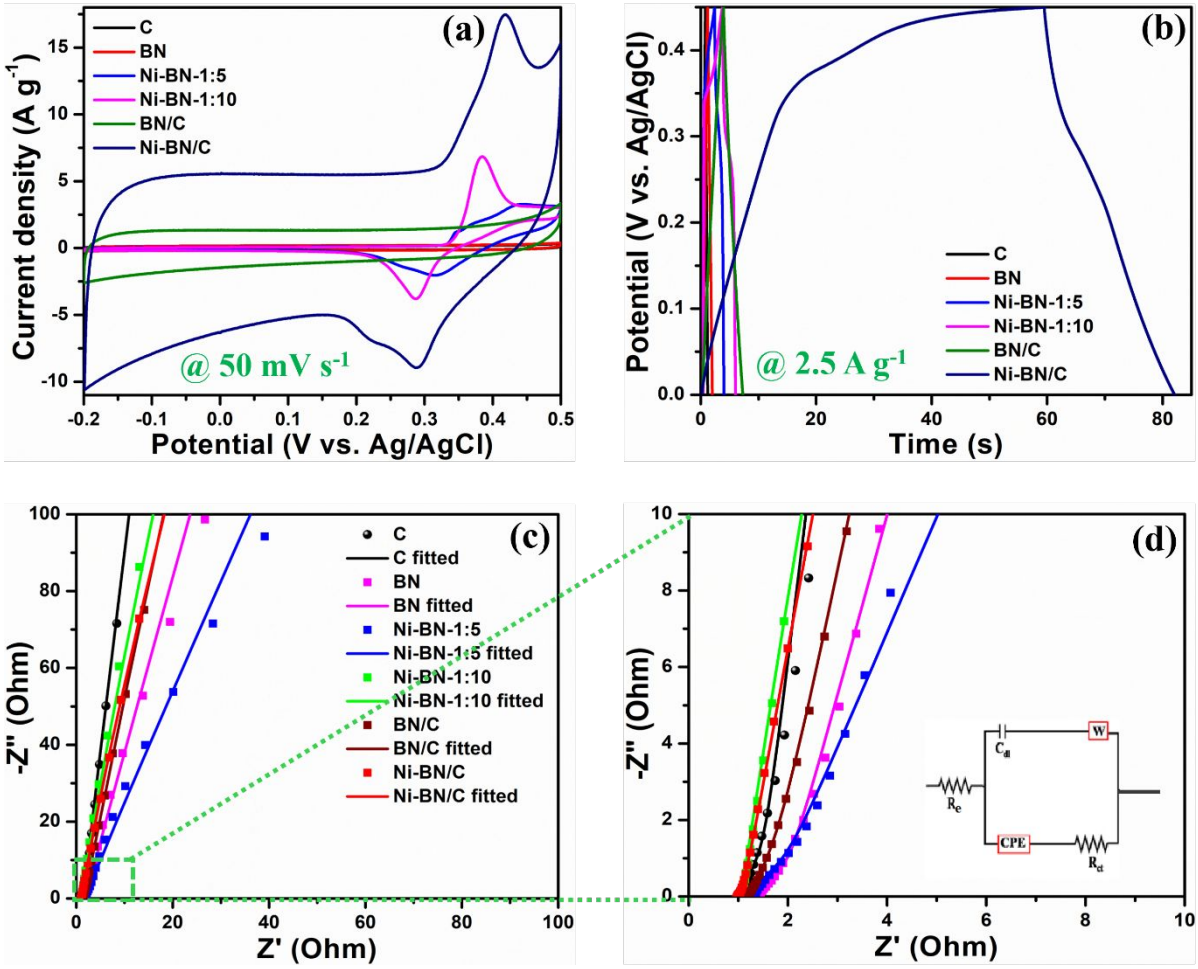

Fig. 6. (a) CV comparison at 50 mV s^{-1}, (b) GCD comparison at 2.5 A g^{-1}, (c, d) comparison of Nyquist plot of the synthesized electrodes, inset of (d) depicts fitting circuit.

Furthermore, the charge transfer mechanism and double-layer capacitance (Cdl) of the synthesized electrodes were investigated using electrochemical impedance spectroscopy (EIS) analysis. Fig. 6(c, d) depicts the unfitted and fitted Nyquist plots which present the imaginary impedance ($-Z''$) versus the real impedance (Z') alongside the corresponding equivalent circuit model [inset of Fig. 6(d)]. In the Nyquist plot, the high-frequency region features a semicircle, representing the charge transfer resistance (R_{ct}), which indicates the efficiency of electron transfer at the electrode–electrolyte interface. The initial segment of the semicircle corresponds to the electrochemical circuit resistance (R_e). In the low-frequency region, the nearly vertical line reflects the capacitive behaviour of the material. The fitted data, summarized in Table 1, reveal that the Ni-BN/C composite exhibits the lowest R_e and low R_{ct} values, confirming its low internal resistance compared to other synthesized electroactive materials. As carbonaceous materials contribute to double-layer capacitance, incorporation of C increases the C_{dl} values of the carbon-based composites. The Ni-BN/C electrode shows the highest C_{dl} value which showed improved capacitive behavior. These results indicate that Ni-

BN/C is associated with the lowest interfacial resistance and most facile charge transfer, designating it as the optimum electrode.

Table 1. Fitted data of Nyquist impedance plot for three-electrode analysis.

Electrodes	R_e (Ω)	R_{ct} (Ω)	C_{dl} (F)
C	1.046	1.669	$0.421e^{-3}$
BN	1.432	1.045	$0.18e^{-3}$
Ni-BN-1:5	1.339	1.138	$0.095e^{-3}$
Ni-BN-1:10	1.039	1.513	$0.33e^{-3}$
BN/C	1.158	3.298	$5.39e^{-3}$
Ni-BN/C	0.976	0.014	$6.717e^{-3}$

The CV profiles of Ni-BN/C at different scan rates are shown in Fig. 7(a) which follow the general trend of supercapacitor electrodes where current response increases with increasing scan rates. Fig. 7(b) shows the corresponding GCD profiles of Ni-BN/C at different current densities which are well in accordance with their CV profiles. The Trasatti method analysis, as shown in Fig. S2, was used to study the capacitive contribution of the synthesized electrodes in terms of EDLC (surface-controlled) and pseudocapacitance (diffusion-controlled). At higher scan rates, the capacitance is primarily dependent on the electrolyte's interaction with the electrode's outer surface, as the electrolyte ions are only accessible to the surface of the electrode material. On the other hand, at slower scan rates, the electrolyte ions can interact unrestrictedly with both the surface and the bulk of the electrode material, making a diffusion-controlled mechanism a predominant one. Following this phenomenon, the EDLC and pseudocapacitance contributions of the synthesized electrodes have been calculated using Trasatti's calculations. It is observed [Fig. S3] that optimum electrode Ni-BN/C is associated with the innovative combination of EDLC (51.2 %) and pseudocapacitance (48.8 %) compared to the other synthesized samples which supports its optimum behaviour. Additionally, Fig. 7(d) shows the almost equal EDLC and pseudocapacitance contribution in terms of the CV area of Ni-BN/C. The EDLC behaviour comes from 2D BN nanosheets and C while pseudocapacitive property arises due to the nickel.

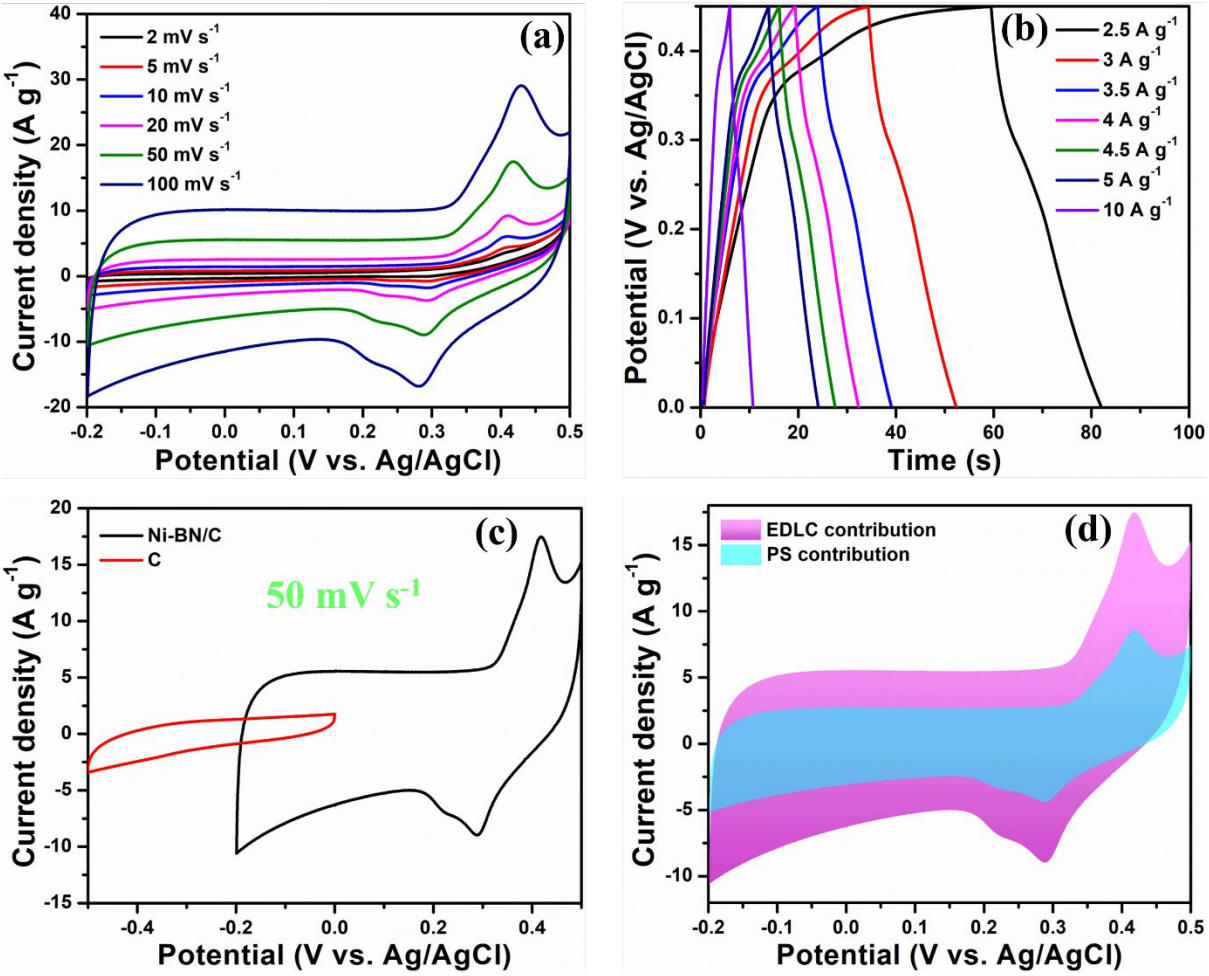

Fig. 7. (a) CV, and (b) GCD profiles of Ni-BN/C, (c) CV scan of Ni-BN/C and C used as positive and negative electrode, respectively in three-electrode setup, and (d) contribution of EDLC and pseudocapacitance (PS) towards the total capacitance of Ni-BN/C.

To further examine the practical applicability of the optimum electrode Ni-BN/C, a two-electrode electrochemical analysis was performed by fabricating an all-solid-state asymmetric supercapacitor (ASSASC) device, with Ni-BN/C serving as the positive electrode and C as the negative electrode. For validation, the electrochemical performances of Ni-BN/C in the positive potential window (-0.2 to 0.5 V) and C in the negative potential window (0 to -0.5 V) are compared in Fig. 7(c) at 50 mV s^{-1} in 1 M KOH in three-electrode analysis. A higher CV area is obtained for C in the negative potential window compared to the positive one, indicating a potential negative electrode. The fabrication of ASSASC device is explained in supporting information S1 and was tested within the voltage range of 0.0 to 1.1 V using PVA/KOH gel polymer (preparation process included in supporting information S1) as separator as well as electrolyte. The PVA-KOH gel was applied over both active materials coated electrodes and dried after sticking together to fabricate the ASSASC device. Fig. S4(a,

c) depict the digital photographs of carbon cloths (2 cm × 2 cm) used as current collector and assembled ASSASC device, respectively. The different parts of the assembled ASSASC device are depicted in Fig. 8(a).

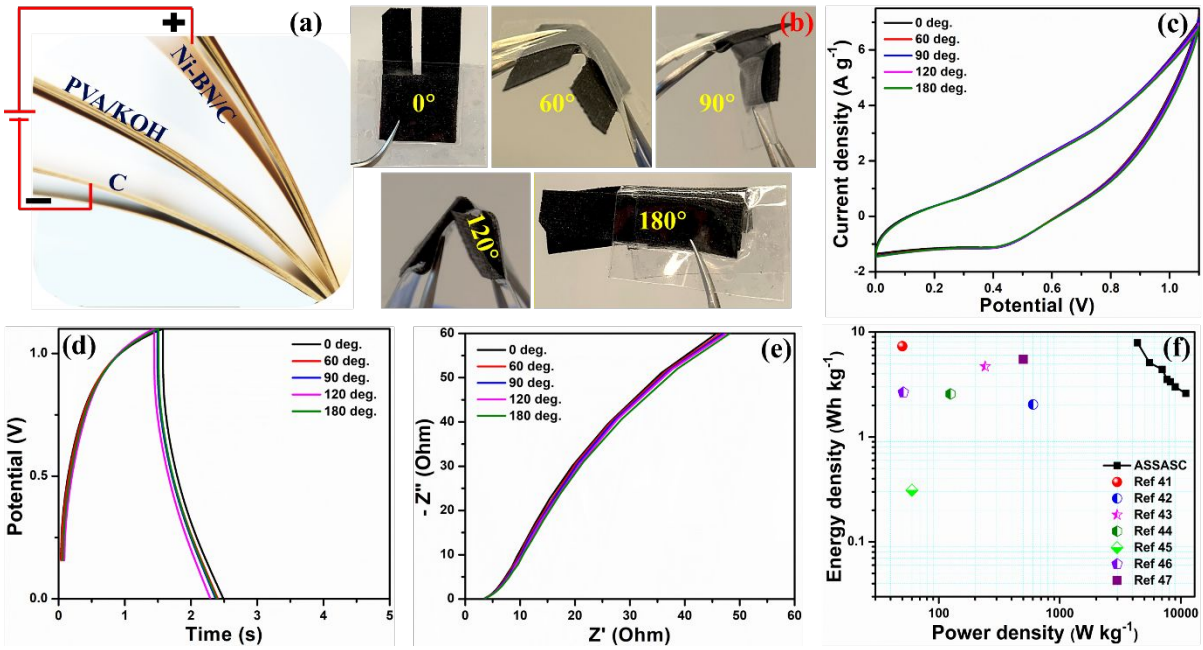

Fig. 8. (a) Schematic representation of the assembled ASSASC device, (b) photographs of the ASSASC device at different bending angles, (c) CV, (d) GCD, and (e) EIS analysis of ASSASC device at different bending angles, and (f) Ragone plot comparing the device performance with previous literatures.

The flexibility of the fabricated device was tested under different bending angles such as 0°, 60°, 90°, 120°, and 180° [Fig. 8(b)] by performing CV at 100 mV s^{-1}, GCD at 4 A g^{-1}, and EIS analysis as exhibited in Fig. 8(c-e), respectively. No obvious change is observed in terms of the CV area or current response for CV analysis, and charging-discharging times for GCD profiles under various bending conditions. Also, the impedance plots are overlapped for different bending states due to having the same interfacial resistance and capacitive behaviour. Thus, a stable electrochemical performance under different bending states indicates a good flexibility of the assembled ASSASC device. The long-term mechanical stability and durability of the flexible device were further tested by performing CV at 100 mV s^{-1}, and EIS analysis under repeated bending cycles. Fig. 9(a) shows the capacitance values obtained from each CV profile after a specific number of bending cycles. After 250 bending cycles, there is no sharp change in capacitance, and the slight deviation after multiple bending tests may arise due to environmental influences. Further, Fig. 9(b) shows the equivalent series resistance (ESR) values obtained from each EIS analysis after specific number of bending cycles. After 250

bending cycles, the increment in resistance is 0.5 % which is almost insignificant. These outcomes attest a good flexibility of the ASSASC device.

The CV curves of the assembled device at different scan rates are shown in Fig. 9(c). The CV curves indicate EDLC as well as pseudocapacitance type charge storage profiles. A redox pair within 0.4 V to 0.7 V arises due to the pseudocapacitive contribution of nickel nanoparticles as explained in the three-electrode study. The GCD profiles at different current densities are shown in Fig. 9(d) which follows a similar trend to the CV profiles. The specific capacitance, energy density, and power density of the ASSASC device were calculated following Eq. S2, S3, and S4, respectively. The device delivered specific capacitance, power density, and energy density of 47 F g^{-1}, 4395.7 W kg^{-1}, and 7.9 Wh kg^{-1}, respectively, at 2 A g^{-1}. Additionally, the device exhibited volumetric energy density of 0.25 mWh cm^{-3} which is suitable for real-time use. Further, the Ragone plot shown in Fig. 8(f) displays that the energy density and power density of this fabricated device are much higher than the previously reported supercapacitor devices (+//–). For example, MXene/carbon nanotube//MXene (7.34 Wh kg^{-1} and 50 W kg^{-1})[41], MXene/metal porphyrin frameworks//MXene/metal porphyrin frameworks (2.04 Wh kg^{-1} and 601.5 W kg^{-1})[42], $Ti_3C_2T_x$//$Ti_3C_2T_x$ (4.7 Wh kg^{-1} and 242 W kg^{-1})[43], paper wasp hive derived activated carbon//paper wasp hive derived activated carbon (2.57 Wh kg^{-1} and 125 W kg^{-1})[44], porous carbon//porous carbon (0.31 Wh kg^{-1} and 60 W kg^{-1})[45], tobacco-derived activated carbon//tobacco-derived activated carbon (2.66 Wh kg^{-1} and 51 W kg^{-1})[46], $Ti_3C_2T_x$//activated carbon (5.5 Wh kg^{-1} and 500 W kg^{-1})[47], porous $Ti_3C_2T_x$/carbon nanotube//porous $Ti_3C_2T_x$/carbon nanotube (CNT) (9.2 Wh kg^{-1} and 96.1 W kg^{-1})[48], and metal organic framework (MOF)/CNT-derived porous carbon//MOF/CNT-derived porous carbon (9.1 Wh kg^{-1} and 3500 W kg^{-1})[49] devices delivered comparable performance to our fabricated device.

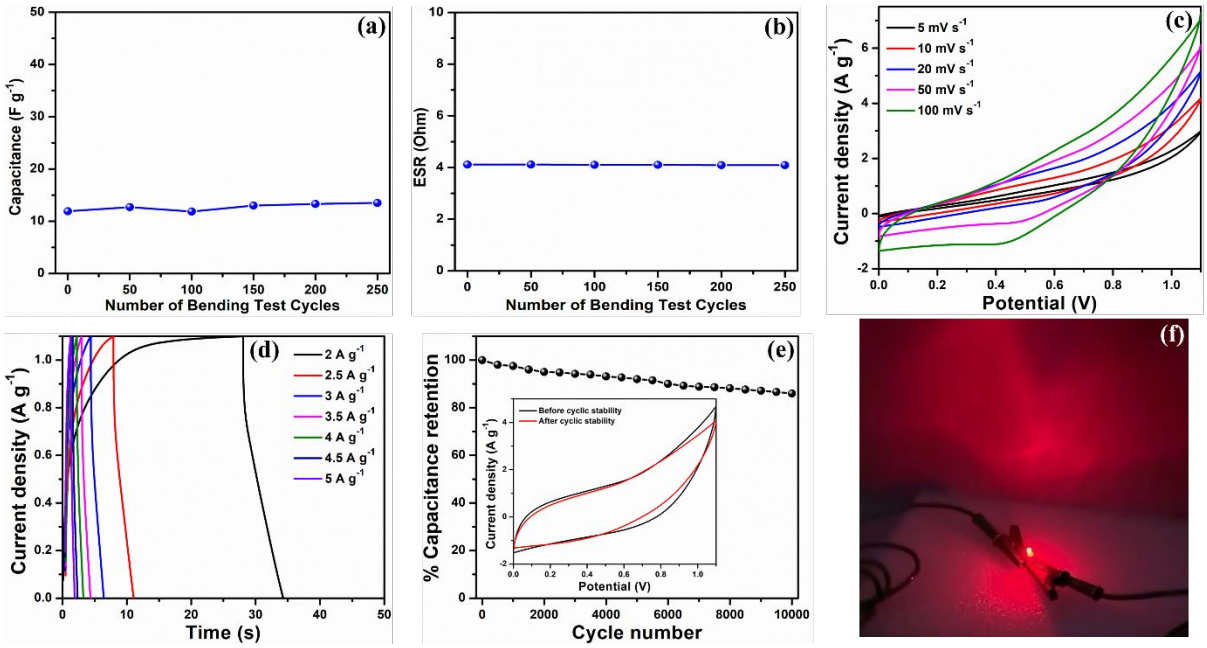

Fig. 9. After long-term bending cycles (a) capacitance corresponding to each CV profile after specific number of bending cycles, and (b) equivalent series resistance (ESR) corresponding to each EIS analysis after specific number of bending cycles; (c) CV profiles of ASSASC device at different scan rates, (d) GCD profiles of the device at different current densities, (e) cyclic stability performance of the device, inset showing the CV profiles before and after cycling test, and (f) digital photograph of lighting up a red led using the assembled ASSASC devices.

A schematic representation of the probable electron transfer pathway within the fabricated device during charging is represented in Fig. 10. The real-time application of a supercapacitor device is also associated with its cyclic life, and the assembled ASSASC device exhibited excellent cyclic stability [Fig. 9(e)] with 86 % specific capacitance retention after 10000 charge-discharge cycles. The electrochemical performance of the device before and after cycling life test is analysed by comparing CV profiles at 200 mV s^{-1} before and after the cyclic stability study shown in the inset of Fig. 9(e). The reduction in CV area is in accordance with the specific capacitance retention after the stability study which can be attributed to the pore saturation after continuous charging-discharging. Also, the stable structural morphology visible in the FESEM image [Fig. S4(b)] of Ni-BN/C after cycling test indicates a stable electrochemical performance of the device. Further, XRD and XPS analysis [Fig. S5] were carried out after a cyclic stability study of Ni-BN/C to confirm the structural integrity and the absence of Ni leaching. The XRD analysis [Fig. S5(a)] confirms that there is no change in the crystal structure of the sample after cycling for 10,000 cycles, as all the characteristic peaks of C, BN, and Ni nanoparticles have been retained. Also, XPS survey scan [Fig. S5(b)] indicates

that the atomic percentages of different elements are almost similar to the initial composition. The deconvoluted spectra of C 1s, B 1s, N 1s, O 1s, and Ni 2p [Fig. S5(c-g)] also shows the presence of similar bonding patterns to those of the initial composite. The slight changes in the peak areas indicate degradation of the sample, which is consistent with the capacitance retention of the sample.

Remarkably, compared to previously documented waste-derived carbon or 2D material-based supercapacitor devices, the specific capacitance and energy density of this fabricated device are significantly higher (Table 2). Furthermore, the ASSASC device exhibited the highest power density among all the mentioned devices, indicating its superiority for real-time applications.

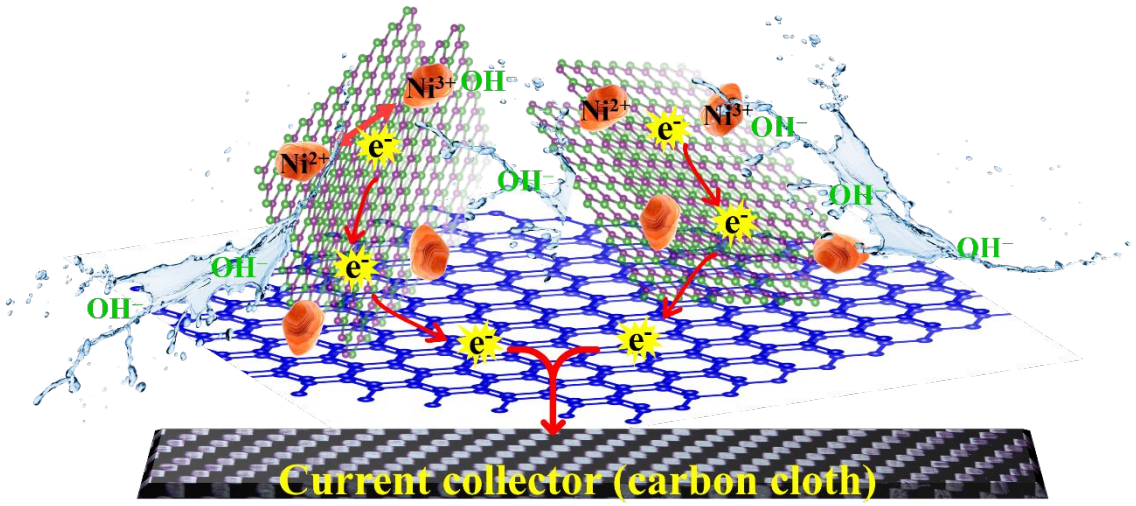

Fig. 10. Schematic of the probable electron transfer mechanism within the fabricated device during charging.

The practical application of the fabricated device was further tested by lighting up the LED. The charging setup of four ASSASC devices connected in series is shown in Fig. S4(d). Fig. 9(f) shows that the assembled devices can glow up a red LED (3 V). This real-time application indicates their efficiency towards future wearable and portable electronic devices. Comprehensively, the excellent electrochemical efficiency of Ni-BN/C as a flexible supercapacitor with high specific capacitance, energy density, and power density can be attributed to the following factors:

(i) The presence of a conducting, porous C matrix facilitates electron transfer.

(ii) Ni nanoparticles incorporate pseudocapacitance to the system by acting as redox active centers (Ni^{2+}/Ni^{3+}).

(iii) The ordered porous structure of conducting C and 2D layers of BN provides a matrix for the Ni particles, which facilitates electrode-electrolyte interaction.

(iv) The synergistic effect of individual components and the presence of different interfaces enhances electrochemical performance by providing facile electron transfer pathways.

Table 2. Comparison of the two-electrode performance of the ASSASC device with previously reported supercapacitor devices.

Supercapacitor devices (+/–)	**Electrolyte**	**Voltage window (V)**	**Current density**	**C (F g-1)**	**E (Wh kg-1)**	**P (W kg-1)**	**% of C retention**	**No. of cycles**	**Ref.**
PWAC//PWAC	ILGPE	1.0	1 mA cm^{-2}	88	2.57	125	72	10000	[44]
Porous carbon//porous carbon	PVA/H_3PO_4	0.8	1 mA cm^{-2}	3.4	0.31	60	88	4000	[45]
TAC//TAC	6 M KOH	0.8	0.5 A g^{-1}	120	2.66	51	100	9000	[46]
$Ti_3C_2T_x$//AC	PVA/Li_2SO_4	1.0	25 mV s^{-1}	46	5.5	500	98	3000	[47]
CAC//CAC	KOH	1.4	0.5 A g^{-1}	106.5	5.15	325	73	11000	[31]
Used cigarette filters-derived porous AC//used cigarette filters-derived porous AC	6 M KOH		0.25 A g^{-1}	52	7.2	127	97.2	5000	[32]
MXene/CNT//MXene	PVA/H_2SO_4	0.8	0.1 A g^{-1}	53	7.34	50	99	5000	[41]
rGO//MXene	1M H_2SO_4	1.1	2 mV s^{-1}	48	8	50	76	1000	[50]
MXene/rGO//MXene/rGO	PVA/H_2SO_4	0.65	0.5 A g^{-1}	65	3.81	163	94.5	10000	[51]
$Ti_3C_2T_x$//$Ti_3C_2T_x$	PVA/H_2SO_4	1.0	0.5 A g^{-1}	151	4.7	242	85	4000	[43]
$Ti_3C_2T_x$-Ar//$Ti_3C_2T_x$-Ar	KOH (30 wt%)	0.7	10 mV s^{-1}	77.5	5.43	700	94.8	10000	[52]
f-MXene//f-MXene	3M H_2SO_4	0.7	1 A g^{-1}	83	6.1	175	89.3	10000	[53]
MXene/MPFs//MXene/MPFs	PVA/H_2SO_4	0.6	0.01 A g^{-1}	40.7	2.04	601.5	95.9	7000	[42]
Ni-BN/C//C	**PVA/KOH**	**1.1**	**2 A g^{-1}**	**47**	**7.9**	**4395.7**	**86**	**10000**	**This work**

**C-specific capacitance; E-energy density; P-power density; PWAC-paper wasp hive derived activated carbon; ILGPE-ionic liquid incorporated gel polymer electrolyte; TAC-tobacco-derived activated carbon; AC- activated carbon; CAC-cigarette filter-derived carbon; CNT-carbon nanotube; rGO-reduced graphene oxide; f-MXene-freeze dried MXene; MPFs-metal porphyrin frameworks.*

4. Conclusion

In summary, nickel was successfully incorporated into BN nanosheets via a facile solid-state method and combined with carbon derived from used cigarette filters for testing its efficiency in a flexible ASSASC device. All the synthesized samples were characterized using various morphological techniques, including FESEM, TEM, EDS, and elemental mapping, as well as

different structural techniques, such as XRD and XPS analysis. Among all the synthesized samples, Ni-BN/C delivered superior electrochemical efficiency as a positive electrode for flexible supercapacitors. The fabricated ASSASC device (Ni-BN/C//C) delivered a high specific capacitance of 47 F g^{-1} with the power density and energy densities of 4395.7 W kg^{-1}, and 7.9 Wh kg^{-1}, respectively, at 2 A g^{-1}. The device also exhibited excellent cyclic stability, with 86% specific capacitance retention after 10,000 charging-discharging cycles. This flexible device also demonstrated superb mechanical stability and durability, withstanding up to 250 bending cycles. These noteworthy results indicate a future direction towards waste to energy and the Ni-BN/C electrode can be used as a potential material for future flexible and wearable energy devices.

Declaration of competing interest

The authors declare that they have no known competing financial interests.

Data availability

The data will be made available upon request.

Acknowledgments

This work was supported by DOE BES award number DE-SC0024611.

Supporting Information

The supporting file contains the experimental section, electrochemical measurement methods, FESEM, EDS, elemental mapping, XRD, XPS, Trasatti method analysis, optical images of the assembled devices, and their charging setup.

References

1. Q. Wang, J. Yan and Z. Fan, *Energy Environmental Science*, 2016, **9**, 729-762.
2. P. Veerakumar, A. Sangili, S. Manavalan, P. Thanasekaran and K.-C. Lin, *Industrial Engineering Chemistry Research*, 2020, **59**, 6347-6374.
3. R. Santos, R. S. Babu, T. Lessa, L. Samyn, R. Vinodh, R. Vivekananth and A. de Barros, *Journal of Industrial Engineering Chemistry*, 2024, **133**, 410-418.
4. R. d. S. dos Santos, R. S. Babu, R. Vinodh, L. M. Samyn, B. G. Pollet, F. Olivera and A. L. F. de Barros, *Diamond Related Materials*, 2023, **136**, 110005.
5. R. Santos, R. S. Babu, M. Devendiran, D. Haddad and A. De Barros, *Materials Letters*, 2022, **308**, 131156.
6. S. De, C. K. Maity, M. J. Kim and G. C. Nayak, *Electrochimica Acta*, 2023, **463**, 142811.
7. S. C. Kishore, R. Atchudan, T. N. Jebakumar Immanuel Edison, S. Perumal, M. Alagan, R. Vinodh, M. Shanmugam and Y. R. Lee, *Energy Fuels,* 2020, **34**, 14958-14967.
8. S. De, J. Florentino, G. Pathiraja, B. R. Gautam and B. P. Bastakoti, *Journal of Materials Chemistry A*, 2025, **13**, 11300-11313.
9. S. De and B. P. Bastakoti, *Journal of Materials Chemistry A*, 2025, **13**, 855-888.

10. S. M. M. Alonzo, M. D. Ashie, G. Pathiraja and B. P. Bastakoti, *Chemical Engineering Journal*, 2025, **505**, 159208.
11. X. Zhang, L. Hou, A. Ciesielski and P. Samorì, *Advanced Energy Materials*, 2016, **6**, 1600671.
12. B. Sahoo, V. Pandey, A. Dogonchi, D. Thatoi, N. Nayak and M. Nayak, *Inorganic Chemistry Communications*, 2023, **154**, 110919.
13. E. Elaiyappillai, R. Srinivasan, Y. Johnbosco, P. Devakumar, K. Murugesan, K. Kesavan and P. M. Johnson, *Applied Surface Science*, 2019, **486**, 527-538.
14. S. Ramanathan, E. Elanthamilan, A. Obadiah, A. Durairaj, J. P. Merlin, S. Ramasundaram and S. Vasanthkumar, *Journal of Materials Science: Materials in Electronics*, 2017, **28**, 16648-16657.
15. M. D. Ashie and B. P. Bastakoti, *Small*, 2024, **20**, 2310927.
16. R. Dahal, R. Srivastava and B. Prasad Bastakoti, *ChemistryOpen*, 2025, **14**, e202400173.
17. B. R. KC, D. Kumar and B. P. Bastakoti, *Journal of Materials Science*, 2024, **59**, 10193-10206.
18. K. Zhang, Y. Feng, F. Wang, Z. Yang and J. Wang, *Journal of Materials Chemistry C*, 2017, **5**, 11992-12022.
19. R. Joy, S. Chahal, V. Biju, P. Kumar and S. Haridas, *ACS Applied Energy Materials*, 2024, **7**, 9766-9774.
20. S. Saha, M. Jana, P. Samanta, N. C. Murmu, N. H. Kim, T. Kuila and J. H. Lee, *Materials Chemistry Physics,* 2017, **190**, 153-165.
21. C. K. Maity, G. Hatui, S. Sahoo, P. Saren and G. C. Nayak, *ChemistrySelect*, 2019, **4**, 3672-3680.
22. C. K. Maity, D. K. Santra, K. Verma, S. Sahoo, S. Cotts, D. Akinwande, V. Berry and G. C. Nayak, *Composites Part B: Engineering*, 2021, **212**, 108728.
23. W. Li, F. Wang, X.-s. Chu, X.-y. Liu and Y.-y. Dang, *Applied Surface Science*, 2021, **560**, 150053.
24. Y. Zhou, J. Xiao-Dong, Z. Wang, H. Y. Xiao, F. Gao and X. T. Zu, *Physical Chemistry Chemical Physics*, 2010, **12**, 7588-7592.
25. Q. Zhuo, X. Liu, O. Jianliang, Z. Fu and X. Xu, *Applied Surface Science*, 2022, **598**, 153719.
26. Q. Chen, Q. Ke, X. Zhao, Y. Feng, Q. Zhao, J. Feng, X. Ge and X. Chen, *Separation Purification Technology,* 2024, **338**, 126552.
27. M. Ikram, J. Hassan, M. Imran, J. Haider, A. Ul-Hamid, I. Shahzadi, M. Ikram, A. Raza, U. Qumar and S. Ali, *Applied Nanoscience*, 2020, **10**, 3525-3528.
28. S. Saha, M. Jana, P. Khanra, P. Samanta, H. Koo, N. C. Murmu and T. Kuila, *ACS applied materials interfaces*, 2015, **7**, 14211-14222.
29. T. Li, X. Jiao, T. You, F. Dai, P. Zhang, F. Yu, L. Hu, L. Ding, L. Zhang and Z. Wen, *Ceramics International*, 2019, **45**, 4283-4289.
30. P. Stigler Granados, L. Fulton, E. Nunez Patlan, M. Terzyk and T. E. Novotny, *International journal of environmental research public health*, 2019, **16**, 1858.
31. Y.-F. Wu, Y.-C. Hsiao, Y.-J. Ou, S. Kubendhiran, C.-Y. Huang, S. Yougbaré and L.-Y. Lin, *Journal of Energy Storage*, 2022, **54**, 105379.
32. R. Bi, S.-K. Pang, K.-C. Yung and L.-K. Yin, *Journal of Electroanalytical Chemistry*, 2022, **925**, 116915.
33. A. M. Al-Enizi, *Colloids Surfaces A: Physicochemical Engineering Aspects*, 2022, **643**, 128775.
34. P. A. M. d. Santos, A. V. Priebbnow, S. Arcaro, R. M. d. Silva, D. A. R. Lopez and A. D. A. L. Rodriguez, *Materials Research*, 2018, **22**, e20180452.
35. M. R. Ahghari, V. Soltaninejad and A. Maleki, *Scientific reports*, 2020, **10**, 12627.
36. N. Srivastava and P. Srivastava, *Bulletin of Materials Science*, 2010, **33**, 653-656.

37. M. W. Alam, A. BaQais, T. A. Mir, I. Nahvi, N. Zaidi and A. Yasin, *Scientific reports*, 2023, **13**, 1328.
38. M. S. Yerdauletov, K. Nazarov, B. Mukhametuly, M. A. Yeleuov, C. Daulbayev, R. Abdulkarimova, A. Yskakov, F. Napolskiy and V. Krivchenko, *Molecules*, 2023, **28**, 5818.
39. J. Qu, Q. Li, C. Luo, J. Cheng and X. Hou, *Coatings*, 2018, **8**, 214.
40. X. Wu, W. Xing, L. Zhang, S. Zhuo, J. Zhou, G. Wang and S. Qiao, *Powder technology*, 2012, **224**, 162-167.
41. X. Shi, F. Guo, K. Hou, G. Guan, L. Lu, Y. Zhang, J. Xu and Y. Shang, *Energy Fuels*, 2023, **37**, 9704-9712.
42. W. Zhao, J. Peng, W. Wang, B. Jin, T. Chen, S. Liu, Q. Zhao and W. Huang, *Small*, 2019, **15**, 1901351.
43. X. Zhang, Y. Liu, S. Dong, J. Yang and X. Liu, *Journal of Alloys Compounds*, 2019, **790**, 517-523.
44. S. Kumar, P. K. Singh, V. D. Punetha, A. Singh, K. Strzałkowski, D. Singh, M. Yahya, S. V. Savilov, P. S. Dhapola and M. K. Singh, *Journal of Energy Storage*, 2023, **72**, 108722.
45. S. Senthilkumar and R. K. Selvan, *ChemElectroChem*, 2015, **2**, 1111-1116.
46. H. Chen, Y.-c. Guo, F. Wang, G. Wang, P.-r. Qi, X.-h. Guo, B. Dai and F. Yu, *New Carbon Materials*, 2017, **32**, 592-599.
47. T.-H. Chang, T. Zhang, H. Yang, K. Li, Y. Tian, J. Y. Lee and P.-Y. Chen, *ACS nano*, 2018, **12**, 8048-8059.
48. P. Zhang, Q. Zhu, R. A. Soomro, S. He, N. Sun, N. Qiao and B. Xu, *Advanced Functional Materials*, 2020, **30**, 2000922.
49. L. Yazhi, L. Gaoran, G. Yi, Y. Yulong and P. Xinsheng, *ACS applied materials interfaces*, 2017, **9**, 14043–14050.
50. A. M. Navarro-Suárez, K. L. Van Aken, T. Mathis, T. Makaryan, J. Yan, J. Carretero-González, T. Rojo and Y. Gogotsi, *Electrochimica Acta*, 2018, **259**, 752-761.
51. D. Jiang, J. Zhang, S. Qin, Z. Wang, K. A. S. Usman, D. Hegh, J. Liu, W. Lei and J. M. Razal, *ACS nano*, 2021, **15**, 5000-5010.
52. R. B. Rakhi, B. Ahmed, D. Anjum and H. N. Alshareef, *ACS applied materials interfaces*, 2016, **8**, 18806-18814.
53. F. Ran, T. Wang, S. Chen, Y. Liu and L. Shao, *Applied Surface Science*, 2020, **511**, 145627.

Data availability

The authors will supply the relevant data in response to reasonable requests.